

Single-LED-pumped, room-temperature, solid-state maser

Michael Newns,¹ Shirley Xu,¹ Mingyang Liu,² Yifan Yu,¹ Zike Cheng,¹ Ziqiu Huang,¹ Max Attwood,³ and Mark Oxborrow¹

¹*Dept. of Materials, Imperial College London, South Kensington, SW7 6AZ, UK*

²*Dept. of Physics, Imperial College London, South Kensington, SW7 6AZ, UK*

³*Dept. of Chemistry, Massachusetts Institute of Technology, Cambridge, MA, 02139, USA*

(*Electronic mail: michael.newns15@imperial.ac.uk; m.oxborrow@imperial.ac.uk)

Through their ability to achieve cryogenic levels of noise performance while operating at room temperature, optically-pumped, solid-state (OPSS) masers show great promise as quantum sensors, oscillators, and amplifiers. We here demonstrate maser oscillation in a microwave cavity containing a crystal of pentacene-doped *para*-terphenyl (ptc:ptp) pumped by a single, chip-scale LED. Here, unlike previous work, the size of the pump source does not dominate the size of the maser system as a whole. This miniaturization is achieved through invasive optical pumping in the form of a waveguide, the tip of which is embedded into the maser crystal. Using experimental measurements combined with microwave and optical simulations, we find that our approach offers at least a factor-of-2 enhancement in cooperativity over end-on optical excitation. We use our simulations to define a figure of merit for maser pumping efficiency, and conclude that there remains significant headroom to improve the performance of ptc:ptp masers through improved optical design.

As quantum devices exploiting stimulated emission, room-temperature masers enable applications that cannot tolerate the severe operating constraints associated with the use of current refrigeration technologies. It is known that masers can amplify weak microwave signals with low noise figures¹, detect extremely weak a.c. magnetic fields², and generate tones at GHz frequencies exhibiting low phase noise^{3,4}. It is also understood^{5,6} that, for these capabilities to persist at room-temperature, the maser must operate at high cooperativity, such that the rate of stimulated emission greatly exceeds the rate of incoherent transitions associated with thermal noise. From a practical standpoint, room-temperature masers are still more cumbersome than semiconductor-based alternatives, due to the size and weight of the electromagnets and/or optical pump light sources required for their operation. This remaining bulk clearly obviates many of the advantages derived from simply overcoming the need for refrigeration.

In the above context, the original series of room-temperature solid-state masers^{7–10}, based on optically-pumped pentacene-doped *para*-terphenyl (ptc:ptp), remain attractive. Unlike masers based on other emitters such as NV centers in diamond, no strong applied DC magnetic field is needed. Furthermore, ptc:ptp masers can sustain high cooperativity in bursts lasting several milli-seconds, which is long enough to be useful in technologically important pulsed applications such as radar and spin-echo EPR. Such a zero-field maser is composed of just two essential parts: the maser cavity itself, and its associated optical pump source.

Hitherto, the size, weight and power ('SWAP') requirements of a ptc:ptp maser have been dominated by the optical pump source, with the cavity typically being at least an order of magnitude smaller in volume. As ptc:ptp masers are limited thermally to pulsed operation, the optical pump source must provide pulses of high instantaneous power lasting ns to ms. Suitable pulsed light sources are bulky and expensive, and those described in the literature (including pulsed solid-state and dye lasers, optical parametric oscillators and Xe flash lamps), have typically occupied volumes on the order of 1 m³ or more (see Fig. 2). The size (and weight)

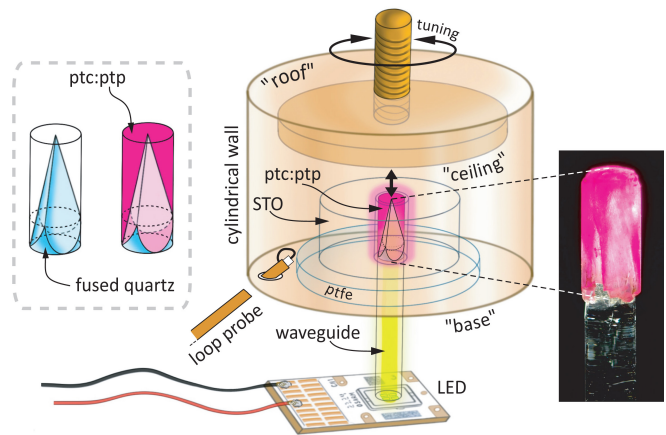


FIG. 1. Geometry of invasively pumped LED maser, including the LED chip, microwave cavity, waveguide and ptc:ptp crystal. The gray-dashed inset box on the then left details the geometry of the waveguide's 3-faceted tip. Displayed on the right is a photo of the invasively pumped ptc:ptp sample used in this work.

of these pump sources clearly limits the practical application of the masers they drive. To be competitive, ptc:ptp masers must offer improved performance over existing room-temperature technologies whilst offering SWAP metrics significantly lower than cryogenic alternatives.

Recently, Ng *et al.* demonstrated a mains-powered, shoebox-sized ptc:ptp maser¹¹ incorporating a miniature pulsed Nd-YAG laser. However, this system still suffers three inefficiencies in common with other (Q-switched and frequency-doubled) Nd:YAG-pumped masers: (1) the 532 nm emission from this laser type lies below (in wavelength) the primary optical-absorption peak at 589 nm for pentacene (in ptp)¹²; (2) Q-switched lasers generating pulses lasting ns provide sufficient instantaneous optical intensity for the rate of optical stimulated emission (from S_1 back down to ground state S_0) to exceed the rate of intersystem crossing ("ISC",

from S_1 to T_2), thus lowering the triplet yield¹³ and (3) due to 0.1% ptc:ptp's short optical penetration depth, shining light onto the outside of a mm-sized ptc:ptp crystal via air-pated optics will fail to illuminate a substantial fraction of its volume¹⁴.

Pumping methodologies that attempt to remedy these issues, particularly the use of invasive optical pumping through Ce:YAG luminescent concentrators (LCs)^{10,15}, have shown significant increases in maser performance compared to air-pated laser excitation. However, the low overall efficiency of the LCs used in these systems to date (typically around 2.5 %¹⁶) has resulted in the need for high-power optical excitation of the LC through either bulky xenon flash lamps^{8,10} or arrays of thousands of LEDs¹⁵.

In this letter, we demonstrate maser action in ptc:ptp using invasive optical pumping from a single, commercially available, chip-scale LED. We find that the same LED (and microwave cavity) is incapable of attaining maser threshold when the LED's output is 'butt-coupled' to the end of a solid ptc:ptp crystal of the same concentration and quality. We use optical ray-tracing simulations combined with finite-element modelling of the microwave cavity mode to show that invasive coupling provides more effective illumination of the ptc:ptp crystal where the a.c. magnetic field is strongest. The resultant maser action produces quasi-continuous maser oscillation (modulated by Rabi-oscillations) characterized by a magnetic quality factor $Q_m \approx 3000$, competitive with previous ptc:ptp masers⁸.

Our results demonstrate a significant miniaturization in the volume of the optical pump source used to drive ptc:ptp masers. Compared to previously reported devices in the literature, our maser system is the first for which the size and weight of its optical pump source do not dominate those of the overall maser system. Fig. 2 plots the approximate volume of most of these pump sources. A notable omission is the work of reference 15; which reports a ptc:ptp maser pumped by an LED-driven Ce:YAG LC, but does not provide sufficient information to estimate the volume that its LEDs occupy. We do know that this maser used 2120 LEDs, each with an output area of $1 \text{ mm} \times 1 \text{ mm}$, thus a total output area of 2120 mm^2 . In comparison, this work used an output area of just 8.32 mm^2 . We attribute this reduction in size to (i) avoiding the loss mechanisms (like escape and re-absorption) associated with Ce:YAG luminescent concentrators¹⁶ and (ii) the effective use of invasive optical pumping.

In this work, a 0.1% ptc:ptp crystal grown atop a fused-quartz waveguide is used as the maser gain media. An additional, non-invasively pumped crystal and waveguide were also fabricated to help quantify the relative benefit of invasive optical pumping. Illustrations of these two geometries are shown in Fig. 3.

Both waveguides were home-manufactured from 13 cm lengths of 5 mm diameter fused-quartz rod using traditional lens making techniques¹⁹, full details of which are given in the supplementary information. On the input end, both waveguides have a polished flat face (oriented at right angles to the rod's axis) to contact and cover the pump LED's flat outputting face. The 'butt-coupled' waveguide has an identical

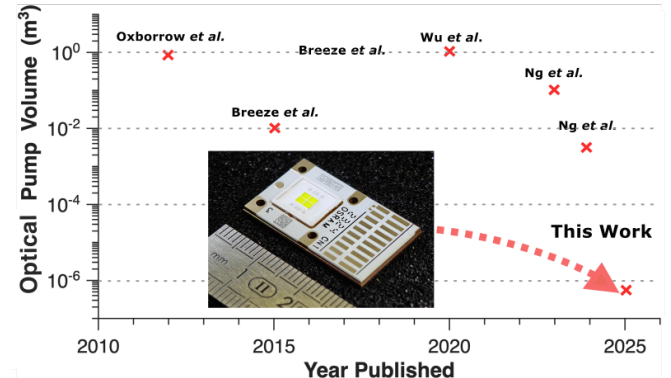


FIG. 2. Approximate optical pump volume reported for key publications on ptc:ptp masers vs year published. The inset photo displays the model of LED used in this work –beside a ruler for scale. References in ascending year are: Oxborrow *et al.*⁷, Breeze *et al.*⁸, Breeze *et al.*¹⁷, Wu *et al.*⁹, Ng *et al.*¹⁸, Ng *et al.*¹¹.

flat face at its other, outputting end, whilst the outputting end of the 'spear-head' waveguide comprises three flat faces coming to a point. The waveguide's length helps isolate the maser crystal from transient magnetic fields generated by the electrical current pulses. Use of magnetic shielding (mumetal) could have permitted a far smaller separation, but was not implemented.

A ptc:ptp crystal was grown atop the outputting end of the spear-head quartz waveguide by the vertical Bridgman method, as has been described in detail in previous work⁹. This method suspends the waveguide inside the glass growth vial in which the ptc:ptp powder is held, allowing a crystal to grow onto and around it. An equivalent solid crystal was grown from the same material and process (less the waveguide) for use with in the butt-coupled configuration.

The maser cavity used in this work, as shown in Fig. 1, closely resembles that used in reference 9. Made of OFHC

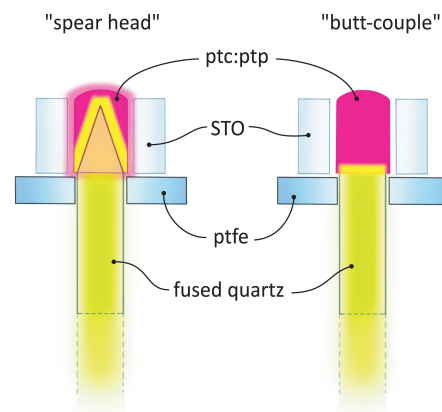


FIG. 3. Meridional cross-sections through the optically-pumped maser's core for the two different pumping geometries considered. In both cases, the STO ring rests on a ptfte washer that itself rests on the cavity's copper base. Yellow shading indicates the extent of the pump light's penetration.

copper, it confines the $TE_{01\delta}$ mode of the SrTiO_3 (STO) dielectric ring that it surrounds. The prepared ptc:ptp crystal and waveguide enter the cavity from below through a concentric hole in the cavity's base plate. The mode's frequency can be adjusted by raising/lowering the height of the cavity's ceiling, and is tuned to the 1.4496 GHz frequency of ptc:ptp's masing $T_X - T_Z$ transition, using a HP 8753A vector network analyser (VNA). An inductive coupling loop is inserted into the cavity, the size and insertion depth of which are chosen to render it under-coupled with respect to the $TE_{01\delta}$ mode. Upon installing a second extremely under coupled loop probe (not shown in Fig. 1), the transmission (S_{21}) between these two probes can be monitored using the VNA, allowing the mode's loaded quality factor to be measured as $Q_L \approx 6000$. To avoid interference/seeding the maser oscillation, the VNA is disconnected from the cavity before the LED is fired.

The optical source is a single LED chip (OSRAM LE CG P2AQ)²⁰ producing high-luminance yellow-green 565–575 nm light, intended for use in video projectors/displays. The LED's outputting surface is rectangular with dimensions 3.2 mm \times 2.6 mm, which can be fully covered by the flat inputting end of each 5-mm quartz waveguide. This interface is covered with a small amount of photo-chemically resistant optical coupling fluid (*viz.* ‘Santovac 5’ polyphenyl ether diffusion-pump oil), filling the gap between the two surfaces. The LED is driven by a home-made circuit that discharges a capacitor (EVOX RIFA 22,000 μF , 63 V, low-ESR electrolytic) through a TTL-controlled, low-on-resistance MOS-FET switch (*viz.* four IRFB3077PbF transistors in parallel driven by a TC4452VAT gate driver) into the LED. In series with the capacitor, a low-inductance 0.02- Ω resistor is placed to allow for output current monitoring, the voltage across which is used to trigger the monitoring Keysight DSOX 6002A oscilloscope. The voltage signal generated by the cavity's primary (most strongly coupled) loop is directly recorded (at 50- Ω input impedance, sampling at 5 GSa s⁻¹) by this scope. A double-DC block is inserted between the cavity and scope as a precaution.

By varying the TTL pulse duration and the voltage to which the capacitor is charged, the pulse energy and duration produced by the LED can be controlled accurately. The available total pulse energy as a function of drive current is shown in Fig. 4. The resulting output optical power profile is determined using a photo-diode (details in supplementary) and is shown at the bottom of Fig. 5 for the two relevant pulse energies.

Using this set-up, maser oscillations of tuneable duration and intensity could be observed on the oscilloscope. When the LED is set to output 6 mJ pulses of 150 μs duration, the strongest maser oscillations were recorded. An example is presented in Fig. 5. In this case, the maser pulse starts approximately 30 μs after the LED is provided with current (at $t = 0$), which is significantly longer than the few μs start up times reported for other ptc:ptp maser systems^{18,21}. Comparing the maser output to the LED output power profile, we can attribute the relatively long start up time to the turn-on delay in the LED output. This trace also shows enveloped power oscillations, attributed to Rabi oscillations, which are indicative of

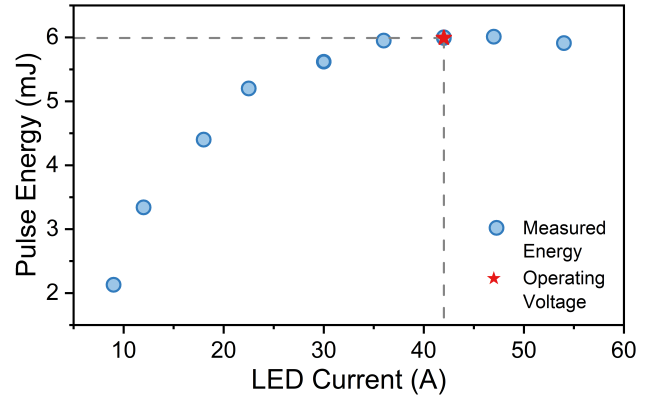


FIG. 4. Detected LED output power vs (maximal) drive current for 150- μs pulses.

the pumping scheme being powerful enough to drive the system into the strong coupling regime¹⁷. These Rabi oscillations decay during the signal, although maser emission is visible throughout the 150 μs pump duration, and even slightly after. This quasi-continuous wave (quasi-CW) operation has only been reported in two other ptc:ptp maser system^{10,15} and indicates that the LED output maintains sufficient power throughout its duration to drive maser oscillation, even as the $T_X : T_Z$ population ratio decreases due to bottlenecking²².

The transient peaks at the start and end of the maser burst are attributed to electromagnetic interference from the current supply. There is no detectable effect in the optical output of the LED, nor do the spectrograms show any evidence of this interference within the band of the maser oscillation. As such, the transients are attributed to inductive interference/crosstalk between the high-current LED driver and the maser's coaxial output channel. More rigorous engineering would be expected to mitigate this.

Reducing the optical output power to 3 mJ over the same pulse duration results in a much weaker maser burst, which starts after approximately 60 μs , and decays more rapidly. The elongated turn-on time, reduced output power and lack of Rabi oscillations at lower pump power (and therefore cooperativity) agrees with the literature^{17,21}. This pump power was in fact found to be the threshold pump power for masing in this system. As the cooperativity is a linear function of optical power⁵, this indicates that the most intense maser bursts (recorded at 6 mJ per pulse) had a cooperativity of approximately 2. For an intrinsic cavity Q_0 of 6,000, this corresponds to a magnetic Q_m of 3,000²³. For comparison, reference 8 reports a ptc:ptp maser with a Q_m of 4,500 in a resonator with a Q_L of 8,900, producing a comparable cooperativity to this system but by using a (large) xenon flash lamp producing a peak optical power of 60–70 W.

When the same system is instead configured with the ptc:ptp solid crystal and ‘butt-coupled’ waveguide, no maser oscillations were observed, even when the pulse energy is increased to 6 mJ over 150 μs . We can infer from this that at least a factor of two enhancement in cooperativity is attained from invasive pumping. This shows that the cooperativity of

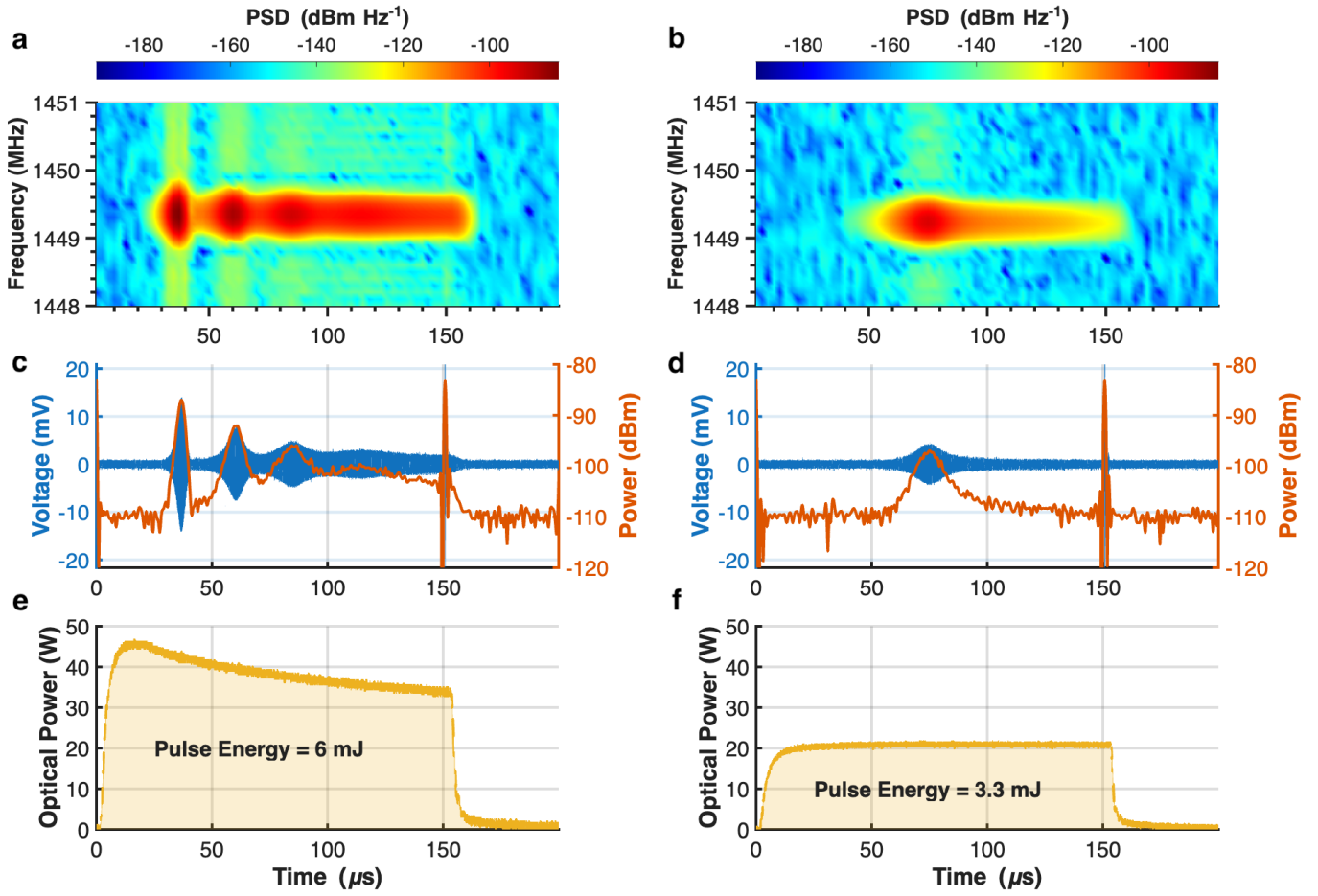


FIG. 5. Maser oscillations produced by the invasively pumped ptc:ptp maser under two different pump intensities. The left column (**a, c, e**) shows the maser bursts recorded at peak LED output power (6 mJ per pulse), whilst the right column (**b, d, f**) shows the maser burst produced when the pump power was reduced to 3.3 mJ per pulse. This was found to be the threshold optical pump power for this sample. The top row (**a, b**) shows the power spectral density (PSD, in dBm·Hz⁻¹), derived from the short-time-Fourier transform of each maser oscillation, taken using Hamming windows containing 2.5×10^4 samples with 50 % overlap and 5×10^4 DFT points, generated in MATLAB R2025B. The middle row (**c, d**) shows the voltage trace as detected by the oscilloscope in blue, and the corresponding RMS power envelope in red, taken as an envelope over windows of 3000 samples. The lower row (**e, f**) shows the time profile of the instantaneous optical power supplied by the LED in each case, with the inset indicating the integrated pulse energy.

a maser is not just a function of the total optical power provided, but is also dependant on how this power is distributed to the crystal. We are thus motivated to adapt the definition the maser cooperativity provided in reference 5 to account for spatially uneven optical pumping:

$$\Gamma = \mu_0 \gamma^2 \sigma^2 \times \frac{\Theta_{\text{ISC}}^{\text{eff}} \times T_1^{\text{eff}} T_2^*}{\omega_{\text{opt}}} \times \frac{Q_L \int_{\Sigma} (\rho_{\text{opt}}(\vec{r}) |B(\vec{r})|^2) dV}{\int_{\text{cav}} |B(\vec{r})|^2 dV}; \quad (1)$$

here, the maser cooperativity Γ is a dimensionless number quantifying the amount by which a maser exceeds threshold ($\Gamma \geq 1$ for masing); μ_0 is the permeability of free space, γ is the electron gyromagnetic ratio, σ^2 is the transition probability matrix element for the maser transition, ω_{opt} is the pump photon angular frequency, $\Theta_{\text{ISC}}^{\text{eff}}$ is the effective the intersystem crossing efficiency, T_1^{eff} is the effective spin-lattice relaxation time, T_2^* is the observed spin-spin relaxation time, Q_L is the (loaded) resonator quality factor, $\rho_{\text{opt}}(\vec{r})$ is the optical en-

ergy density at position \vec{r} in the crystal Σ , $B(\vec{r})$ is the resolved component of the magnetic flux density interacting with the sample at position \vec{r} , and $B(\vec{r})$ is the complete magnetic flux density at same.

From the point of view of optimising the cooperativity of a given maser system through optical engineering, the integral in the numerator of the final factor of (1) is the main quantity of interest. It is clear that increasing the value of this integral is best achieved by maximizing the optical energy density in those areas of the maser crystal where the RF magnetic field is strong.

To better understand our results in this context and direct further improvements, we simulate the spatial distribution of the optical energy density absorbed by the ptc:ptp crystal, $\rho_{\text{opt}}(\vec{r})$ (in units of W/mm³), for both the invasive and butt-coupled configurations, using PVtrace open source ray tracing software²⁴⁻²⁷. In tandem with the optical engineering, RF simulations of the a.c. magnetic field generated by the TE₀₁₈

mode are conducted using eigen-frequency analysis of a (lossless) model of the cavity in COMSOL Multiphysics (version 6.0), resulting in a normalised distribution of \tilde{B} throughout the cavity. Details of the simulation methodology for both the optical and RF simulations are given in the supplementary information.

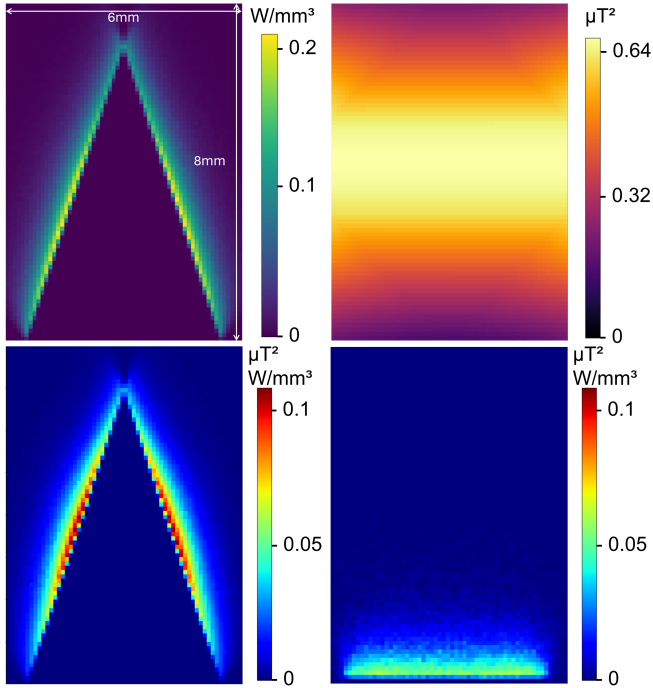


FIG. 6. Top left: Simulation of the normalized absorbed energy density $\tilde{\rho}_{\text{opt}}$, in the invasively pumped ptc:ptp sample, using PVtrace.

Top right: COMSOL simulation of the normalized $|\tilde{B}|^2$ inside the bore of the STO dielectric resonator. These are projected from the full 3D data sets. The integral over the displayed region for both $\tilde{\rho}_{\text{opt}}$ and $|\tilde{B}|^2$ is normalized to 1 W of total absorbed optical power, and 1 J of total magnetic flux energy, respectively. Bottom panel: Comparison of the local value of $\tilde{\rho}_{\text{opt}} \times |\tilde{B}|^2$ for invasive pumping (left) and butt-coupling (right).

Examples of the simulated (normalized) distributions of $\rho_{\text{opt}}(\vec{r})$, $|B(\vec{r})|^2$ and $\rho_{\text{opt}}(\vec{r}) \times |B(\vec{r})|^2$ are shown in Fig. 6. Combining optical and RF simulations in this manner allows one to both map the distribution of $\rho_{\text{opt}}(\vec{r}) \times |B(\vec{r})|^2$ and to estimate the normalised utilization or overlap factor defined as: $\Delta = \int_{\Sigma} (\tilde{\rho}_{\text{opt}}(\vec{r}) |\tilde{B}(\vec{r})|^2) dV$, which provides a measure of the overall efficiency of the pumping geometry simulated. This term evaluates to $\Delta = 2.26 \times 10^{-3} \text{ T}^2 \text{W}$ for the butt-coupled configuration, while for the invasively pumped configuration it evaluates to $\Delta = 4.60 \times 10^{-3} \text{ T}^2 \text{W}$, demonstrating a 2.08 times improvement with invasive pumping. It should be noted that this is despite a large reduction in the available volume of ptc:ptp crystal. Given that the invasively pumped variant was found to have a cooperativity of approximately 2, this result implies that the butt-coupled variant should lie just below the $\Gamma = 1$ threshold for maser oscillation, consistent with experiment.

We further simulate the limit of completely uniform optical excitation (*i.e.*, $\rho(\vec{r}) \equiv \bar{\rho}_{\Sigma}$), and find this to provide worse performance than that provided by our (imperfect) invasive pumping geometry, with the above integral evaluating to $\Delta = 4.56 \times 10^{-3} \text{ T}^2 \text{W}$. We can thus conclude that, for OPSS masers, in the limit where the total optical power (intensity) available is insufficient to bleach (and thus optical pump) the whole crystal, it is advantageous to illuminate a smaller region, accessible through invasive waveguiding, where the a.c. magnetic flux density is highest. We also note that, on an absolute scale, looking at Fig. 6, the ptc:ptp gain medium is poorly utilized, suggesting substantial headroom for improvement through pump optics capable (somehow) of supplying light more uniformly throughout the crystal's volume.

In conclusion, we have demonstrated maser oscillations in a solid-state, room-temperature maser that is invasively pumped through a quartz waveguide by a single, chip-scale LED. We estimate the cooperativity of this maser to be approximately 2, and find that it can produce quasi-CW maser oscillations with features competitive with previously reported embodiments. This system is the smallest room-temperature maser yet reported in the literature, and is the first in which the optical pump source is not a limiting component in terms of the maser's overall volume and weight. We find that the same maser system is incapable of achieving masing when butt-coupled to a similar waveguide. Through a novel coupled RF-optical simulation approach, we estimate that the enhancement in cooperativity achieved by the invasive pumping is approximately a factor of 2 compared to end-on pumping, and even a slight improvement over perfectly uniform pumping. Our analysis strongly motivates attempts to further improve the pump optics towards providing more-capable and lower-SWAP designs of OPSS maser.

I. ACKNOWLEDGMENTS

We thank Ben Gaskill of Gaskill Quartz Ltd., London, for manufacturing the STO ring resonator used in this work.

II. BIBLIOGRAPHY

1. R. C. Clauss and J. S. Shell, *Ruby masers*, edited by M. S. Reid (JPL Deep Space Communications And Navigation Series, Jet Propulsion Laboratory, 2008).
2. H. Wu, S. Yang, M. Oxborrow, M. Jiang, Q. Zhao, D. Budker, B. Zhang, and J. Du, "Enhanced quantum sensing with room-temperature solid-state masers," *Science Advances* **8**, eade1613 (2022).
3. H. M. Goldenberg, D. Kleppner, and N. F. Ramsey, "Atomic hydrogen maser," *Physical Review Letters* **5**, 361 (1960).
4. Y. Varshavsky, O. Zgadzai, and A. Blank, "Solid-state maser with microwave output power at moderate cryogenic temperatures," *arXiv preprint arXiv:2504.06846* (2025).
5. M. Oxborrow and US patent US9608396B2, "Maser assembly," (2012).
6. A. Sherman, O. Zgadzai, B. Koren, I. Peretz, E. Laster, and A. Blank, "Diamond-based microwave quantum amplifier," *Science Advances* **8**, eade6527 (2022).
7. M. Oxborrow, J. D. Breeze, and N. M. Alford, "Room-temperature solid-state maser," *Nature* **488**, 353–356 (2012).

⁸J. Breeze, K. J. Tan, B. Richards, J. Sathian, M. Oxborrow, and N. M. N. Alford, “Enhanced magnetic Purcell effect in room-temperature masers,” *Nature Communications* **6**, 1–6 (2015).

⁹H. Wu, H. Wu, S. Mirkhanov, W. Ng, K.-C. Chen, Y. Xiong, Y. Xiong, and M. Oxborrow, “Invasive optical pumping for room-temperature masers, time-resolved EPR, triplet-DNP, and quantum engines exploiting strong coupling,” *Optics Express* **28**, 29691–29702 (2020).

¹⁰H. Wu, X. Xie, W. Ng, S. Mehanna, Y. Li, M. Attwood, and M. Oxborrow, “Room-Temperature Quasi-Continuous-Wave Pentacene Maser Pumped by an Invasive Ce:YAG Luminescent Concentrator,” *Physical Review Applied* **14** (2020).

¹¹W. Ng, Y. Wen, M. Attwood, D. C. Jones, M. Oxborrow, N. M. N. Alford, and D. M. Arroo, “‘Maser-in-a-shoebox’: A portable plug-and-play maser device at room temperature and zero magnetic field,” *Applied Physics Letters* **124**, 44004 (2024).

¹²Q. Ai, P. Chen, Y. Feng, and Y. Xu, “Growth of Pentacene-Doped p-Terphenyl Crystals by Vertical Bridgman Technique and Doping Effect on Their Characterization,” *Crystal Growth and Design* **17**, 2473–2477 (2017).

¹³K. Takeda, T. Yamamura, A. Kagawa, and M. Kitagawa, “Enhancement of efficiency in photo-excitation to the triplet state by laser-pulse reshaping,” *Journal of Magnetic Resonance* **174**, 310–313 (2005).

¹⁴K. Takeda, K. Takegoshi, and T. Terao, “Zero-field electron spin resonance and theoretical studies of light penetration into single crystal and polycrystalline material doped with molecules photoexcitable to the triplet state via intersystem crossing,” *Journal of Chemical Physics* **117**, 4940–4946 (2002).

¹⁵S. Long, L. Lopez, B. Ford, F. Balembois, R. Montis, W. Ng, D. Arroo, N. Alford, H. Torun, and J. Sathian, “LED-pumped room-temperature solid-state maser,” *Communications Engineering* **4** (2025).

¹⁶J. Sathian, J. D. Breeze, B. Richards, N. M. Alford, and M. Oxborrow, “Solid-state source of intense yellow light based on a Ce:YAG luminescent concentrator,” *Optics Express* **25**, 13714–13727 (2017).

¹⁷J. D. Breeze, E. Salvadori, J. Sathian, N. McN. Alford, and C. W. Kay, “Room-temperature cavity quantum electrodynamics with strongly coupled Dicke states,” *npj Quantum Information* **3** (2017).

¹⁸W. Ng, X. Xu, M. Attwood, H. Wu, Z. Meng, X. Chen, and M. Oxborrow, “Move Aside Pentacene: Diazapentacene-Doped para-Terphenyl, a Zero-Field Room-Temperature Maser with Strong Coupling for Cavity Quantum Electrodynamics,” *Advanced Materials* **35**, 2300441 (2023).

¹⁹F. Twyman, *Prism and Lens Making, Second Edition: A Textbook for Optical Glassworkers* (Taylor and Francis, 1988).

²⁰OSRAM OSTAR™ Projection Power, LE CG P2AQ, ams-OSRAM AG (2025).

²¹E. Salvadori, J. D. Breeze, K. J. Tan, J. Sathian, B. Richards, M. W. Fung, G. Wolfowicz, M. Oxborrow, N. M. N. Alford, and C. W. Kay, “Nanosecond time-resolved characterization of a pentacene-based room-temperature MASER,” *Scientific Reports* **7**, 1–8 (2017).

²²H. Wu, W. Ng, S. Mirkhanov, A. Amirzhan, S. Nitnara, and M. Oxborrow, “Unraveling the Room-Temperature Spin Dynamics of Photoexcited Pentacene in Its Lowest Triplet State at Zero Field,” *Journal of Physical Chemistry C* **123**, 24275–24279 (2019).

²³A. E. Siegman, *Microwave Solid-state Masers* (McGraw-Hill electrical and electronic engineering series, 1964).

²⁴D. J. Farrell, *Characterising the Performance of Luminescent Solar Concentrators*, Ph.D. thesis, Imperial College London (2008).

²⁵D. J. Farrell, “pvtrace: Optical ray tracing for luminescent materials and spectral converter photovoltaic devices,” <https://github.com/danieljfarrell/pvtrace>.

²⁶S. Verma, D. J. Farrell, and R. C. Evans, “Ray-trace modeling to characterize efficiency of unconventional luminescent solar concentrator geometries,” *ACS Applied Optical Materials* **1**, 1012–1025 (2023).

²⁷Shomik Verma, “Pvtrace-Sv,” <https://github.com/shomikverma/pvtrace-sv>.

²⁸K. A. Nelson, D. Lutz, M. Fayer, and L. Madison, “Laser-induced phonon spectroscopy: optical generation of ultrasonic waves and investigation of electronic excited-state interactions in solids,” *Physical Review B* **24**, 3261 (1981).

III. SUPPLEMENTARY INFORMATION

A. Waveguide Shaping

A cut 13 cm length of rod was held with various home-made polishing guides and pressed against the surface of a rotating grinding/polishing wheel, onto which progressively finer grades of abrasive paper were attached. The final polishing of each face/facet was done against a napped cloth impregnated with 3- μ m diamond paste on a similar wheel. On the input end, both waveguides have a polished flat face (oriented at right angles to the rod’s axis) to contact and cover the pump LED’s flat outputting face. The ‘butt-coupled’ waveguide has an identical flat face at its other, outputting end. The outputting end of the spear-head waveguide in contrast comprises three flat faces (facets), like the apex of a triangular pyramid (tetrahedron), but with a elliptical edge where each of these facets meets the waveguide’s cylindrical shank (see Fig. 1). The waveguide’s length helps isolate the maser crystal from transient magnetic fields generated by the electrical current pulse flowing through the LED; the length could certainly be reduced by placing one or several layers of magnetic (mumetal) shielding between the LED and maser crystal, but this sophistication was not implemented here.

B. LED Optical Characterization and Set-up

As a precaution against overheating during sustained pulsed operation, the LED module is mounted with thermally-conductive paste onto the top of a metallic heatsink. The drive currents used in this work are significantly above the maximal surge current (14 A) stated in the LED’s datasheet²⁰. The risk of damage was mitigated by using short pulse durations (150 μ s) and a low duty cycle of 1 pulse per second. This allowed for hours of above-threshold pulsed operation without LED failure.

The optical output from the LED (both overall energy dose and instantaneous power as a function of time) received by the maser crystal is estimated using a combination of an ES245C pyroelectric energy meter and a DET-200 (modern equivalent: DET100A2) silicon photodetector, both from Thorlabs. The flat receiving surface of the ES245C is placed just above the flat outputting face of the butt coupled 5-mm fused-quartz waveguide (*i.e.*, the butt-coupled geometry but without a maser crystal) with air in between. The vertical scale of the corresponding time profile recorded by the DET-200 (used as an uncalibrated linear power meter of sufficient bandwidth) is then adjusted such that its integral equals the measured total pulse energy from the energy meter. This allows for the instantaneous absorbed power as a function of time to be determined, as shown at the bottom of Fig. 5 for two pulse energies (and thus thus two different voltages on the LED-driver’s capacitor).

Such a measurement of the optical energy/power (with an air gap between the outputting face and energy meter) inevitably underestimates the energy fraction of the light that will actually get transmitted into the ptc:ptp maser crystal

(whose refractive index lies closer to that of fused quartz compared to that of air). To correct for this, ray tracing is used to determine (a) the fraction of the LED's output that arrives at the surface of the ES245C energy meter and (b) the fraction of same that gets absorbed by the ptc:ptp crystal for both the (i) butt-coupled and (ii) invasive spear-head geometries. The ray tracing takes into account both reflections from all interfaces and the escape of pump light from the crystal (upon passing through the sections of it that are too thin to completely absorb the pump light). Although the invasive geometry does better than a butt couple at avoiding the retro-reflection of pump light back into the waveguide, more pump light is lost by escape through the thin sections of the crystal where the spear head's flat faces meet the waveguide outer cylindrical surface. The ratio of the fractions (b)/(a) provides a correction factor, allowing the true amount (*i.e.*, energy and thus number of photons) of light absorbed by the ptc:ptp crystal to be inferred from the energy meter's reading. We find the factor to be (i) 1.07 for the butt couple and (ii) 1.01 for the spear head, these are not corrected for in the data in Fig. 5.

C. Optical and RF simulation

Within our simulation, we treat the LED as a flat rectangular lambertian light source, emitting through a layer of optical coupling liquid into the waveguide. Light from the LED that is successfully captured by the waveguide then propagates along it by total internal reflection until it meets the waveguide's terminating ptc:ptp crystal. In our simulation, we assume that 0.1% ptc:ptp is a linear optical (ignoring bleaching effects) absorber (obeying the Beer-Lambert law in the direction of optical transport), where the effective absorp-

tion coefficient of the light emitted by the LED is $\approx 2 \text{ mm}^{-1}$ given the LED's output spectrum²⁰ and ptc:ptp's absorption spectrum^{18,28}. Neither the birefringence of *para*-terphenyl nor the anisotropy (both direction and polarization dependence) of pentacene's optical absorption (when dissolved as a substitutional dopant in the former) were explicitly included. In our invasive-pumping simulations, a simplified two-faced wedge geometry was adopted instead of the experimental three-faced spear-head geometry (though with equivalent aspect ratios). This choice was made to preserve clear and intuitive 2D projections of the absorbed optical energy density, as the non-parallel facets of the three-faced geometry complicate direct visual presentation. Physically, this simplification is not expected to significantly effect the optical coupling efficiency, since absorption at each emitting facet occurs without total internal reflection and the ray distribution retains azimuthal symmetry.

RF modelling is conducted in COMSOL multiphysics v6.0, using the RF module to conduct eigen frequency analysis of a simplified model of the cavity internals. The STO resonator is modelled as a lossless dielectric with $\epsilon_r = 318$, supported by a PTFE stand (internal material parameters), with perfect-electric-conductor boundary conditions simulating the copper cavity's walls. No attempt is made to electromagnetically simulate the ptc:ptp crystal, waveguide or coupling loops, as these are non magnetic and not found to significantly effect the mode. The simulated data set is used to extract a high resolution interpolation of $|B|^2$ in the central bore of the dielectric resonator. This distribution is normalised through COMSOL's in-built normalization process. We therefore consider that $B(\vec{r}) = \mathbf{B}(\vec{r})$, this assumes that the ptc:ptp crystal is single, and that all ptc molecules experience the same transition dipole moment $\mathbf{B}(\vec{r}) \cdot \hat{\mu}(\vec{r}) = B(\vec{r})$.